Journal of Fluids and Structures (1997) **11,** 665–691

COMPUTATION OF NON-STATIONARY SHOCK-WAVE/CYLINDER INTERACTION USING ADAPTIVE-GRID METHODS

D. Drikakis, D. Ofengeim

UMIST, Department of Mechanical Engineering, PO Box 88, Manchester M60 1QD, U.K.

E. Timofeev

Ioffe Physical-Technical Institute, Russian Academy of Sciences, Polytekhnicheskaya 26, St. Petersburg 194021, Russia

AND

P. Voionovich

Advanced Technology Center, P.O. Box 29, St. Petersburg, Russia

(Received 4 June 1996 and in revised form 9 June 1997)

A numerical study of shock wave propagation over a cylinder is presented. Hybrid, structured-unstructured adaptive grids are employed for the numerical solution of the Euler and Navier-Stokes equations. A second-order Godunov-type scheme is employed for the discretization of the inviscid fluxes, while central differences are used for the viscous terms. The time integration is obtained by a second-order prediction-corrector scheme. Simulation of the unsteady gasdynamic phenomena around the cylinder is obtained at different incident-shock Mach numbers. The shock-wave diffraction over the cylinder is investigated by means of various contour plots, as well as pressure and skin friction distributions. The calculations reveal that the Euler solutions are very close to the Navier-Stokes ones in the first half of the cylinder, but large differences between the two solutions exist in the second half of the cylinder and the wake of the flow field, where strong viscous-inviscid interaction occurs.

1. INTRODUCTION

Interaction of shock waves with obstacles has attracted the interest of many theoretical, numerical and experimental studies. This interest is largely motivated by the understanding of the physics of non-stationary gas-dynamic phenomena, as well as from the fact that oblique reflection and diffraction appear in explosion dynamics (Glass & Sislian 1994). The gas-dynamic phenomena may include several types of non-stationary interactions such as shock-obstacle, shock-shock and viscous-inviscid interactions.

0889–9746/97/060665 + 28 $25.00/fl970104

Whitham (1957) has developed an approximate theory for the dynamics of shock waves and applied this theory to the description of shock diffraction on wedges and corners. Bryson & Gross (1961) extended Whitham's theory to two- and three-dimensional bodies such as cylinders and spheres. They also performed shock tube experiments to check the accuracy of the theory and to illustrate the diffraction flow patterns. Their theoretical predictions were in very good agreement with the experimental data. Similar studies were also performed by Heilig (1960), Syshchikova *et al.* (1967), Takayama & Kawauchi (1979), Takayama & Ito (1985). An interferometric investigation of a planar shock wave over a semi-circular cylinder was also presented by Kaca (1988).

On the other hand, due to the recent advancements of Computational Fluid Dynamics (CFD), especially in the field of shock-capturing schemes and unstructured adaptive grids, very accurate simulation of non-stationary gas-dynamic phenomena can be achieved. Regarding the numerical algorithm development, the simulation of shock propagation and unsteady interaction with structures pose significantly greater demands than those required by traditional shock capturing schemes [e.g., Harten 1983], which are only intended to produce steady, non-oscillatory shocks. Past simulations of shock-wave propagation over long distances relied on either a fixed-mesh structured grid approach (Glaz *et al.* 1985) or sliding refined zones, intended to surround the shocks continuously with a finer mesh than elsewhere in the domain (Berger & Oliger 1984). Baum & Löhner (1994) carried out inviscid simulation of shock propagation over a box suspended above a rigid elevated surface. They used unstructured grids in conjunction with finite-element methods and high-resolution monotonicity-preserving algorithms (Löhner *et al.* 1988; Löhner 1987). Inviscid simulation of complicated flow fields involving strong shock waves has been presented by Woodward & Colella (1984), Colella & Glaz (1985), as well as by Glaz *et al.* (1985). Yang *et al.* (1987) studied the non-stationary shock-wave reflection generated by a blast shock wave impinging on a circular cylinder. They used structured grids and a second-order hybrid upwind method to solve the compressible Euler equations. Yang *et al.* (1993) studied shock wave reflection over a circular cylinder in a dusty gas. Their simulation was based on the two-phase Euler equations, unstructured grids, and a second-order Godunov-type scheme. Drikakis & Tsangaris (1993) have also developed high-order upwind schemes for the simulation of both inviscid and viscous flows with strong shock waves over bluff bodies including real gas effects. Ofengeim *et al.* (1993) have studied, on the basis of Euler equations, the pressure load on the cylinder surface during the diffraction of strong shock waves, while Glass *et al.* (1989) have provided direct comparison of structured-grid inviscid calculations to experiments for the cases of half-diamond and semi-circular cylinders. All the foregoing studies were focused on either the validation of the Euler unstructured-grid algorithms or the investigation of shock-wave phenomena at certain Mach numbers on the basis of *inviscid* simulation.

The aim of the present paper is to study the propagation of shock waves over a cylinder using both the Euler and Navier-Stokes equations, and more specifically to examine the viscous effects at various Mach numbers by comparing the inviscid and viscous calculations. The emphasis of the paper is on the results rather than the algorithms employed, and therefore the presentation and validation of the algorithm is kept to a sufficient, but not exhaustive, depth. In Section 2 the numerical method is described, while in Section 3 the results from the numerical study are presented. Finally, in Section 4 conclusions from the present research are drawn.

2. MATHEMATICAL MODELLING

2.1. Governing Equations

The numerical method employed has been presented in a very brief form by Beryozkina *et al.* (1996). In this paper a preliminary validation of the method was presented. A detailed description of the method is given below.

The governing equations are the two-dimensional Navier-Stokes equations, which are written in an integral form as follows:

$$\frac{\partial}{\partial t}\oint_{\Omega}\mathbf{U}\,\mathrm{d}\Omega+\oint_{S}((\mathbf{F}_x^c+\mathbf{F}_x^v)n_x\,\mathrm{d}S+(\mathbf{F}_y^c+\mathbf{F}_y^v)n_y\,\mathrm{d}S)=\mathbf{0} \tag{1}$$

where

$$\mathbf{U}=\begin{Bmatrix}\rho\\ \rho u_x\\ \rho u_y\\ e\end{Bmatrix},\qquad \mathbf{F}_x^c=\begin{Bmatrix}\rho u_x\\ \rho u_x^2+p\\ \rho u_y u_x\\ (e+p)u_x\end{Bmatrix},\qquad \mathbf{F}_y^c=\begin{Bmatrix}\rho u_y\\ \rho u_x u_y\\ \rho u_y^2+p\\ (e+p)u_y\end{Bmatrix},$$

$$\mathbf{F}_x^v=\begin{Bmatrix}0\\ \tau_{xx}\\ \tau_{yx}\\ \tau_{xx}u_x+\tau_{yx}u_y+k(\partial T/\partial x)\end{Bmatrix},\qquad \mathbf{F}_y^v=\begin{Bmatrix}0\\ \tau_{yx}\\ \tau_{yy}\\ \tau_{yx}u_x+\tau_{yy}u_y+k(\partial T/\partial y)\end{Bmatrix}$$

where $\mathbf{u}=(u_x, u_y)$ is the velocity vector, while p, ρ, T and e are the pressure, density, temperature and total energy, respectively. The shear stress components are represented by τ_{xx}, τ_{yx} and τ_{yy}, while $k=\mu C_p/\mathrm{Pr}$ is the heat conductivity coefficient (C_p and Pr are the specific heat at constant pressure and Prandtl number, respectively). The viscosity coefficient μ is calculated by the Sutherland's law. Ω represents a control volume bounded by the surface S, while $\mathbf{n}=(n_x, n_y)$ is the unit normal vector [Figure 1(a)].

2.2. Numerical Method

The numerical method used here is the extension of the algorithm developed by Fursenko *et al.* (1995) to simulate unsteady inviscid flows using adaptive unstructured grids. Preliminary validation of the method in viscous flows was performed by Beryozkina *et al.* (1996). In the present work the viscous flow solver is extensively validated and subsequently used for the study of shock-wave propagation phenomena over a cylinder. The main goal of the paper is the investigation of the flow phenomena rather than the algorithmic issues, but a description of the method is given below.

In viscous flows the implementation of unstructured grids in the near wall region results in very elongated triangles, which lead to a significant reduction of the CFL number. It has been found that the use of a structured grid in the near-wall region facilitates the implementation of implicit schemes which subsequently improve the efficiency of the numerical solution in the boundary layer region (Beryozkina *et al.* 1996). Therefore, in the present work a hybrid structured-unstructured grid was implemented. A structured grid (quadrilateral elements) covers a region around the solid surface, while an adaptive unstructured grid based on triangular elements covers the rest of the domain [Figure 1(b)]. A geometric rule has been used in order to define

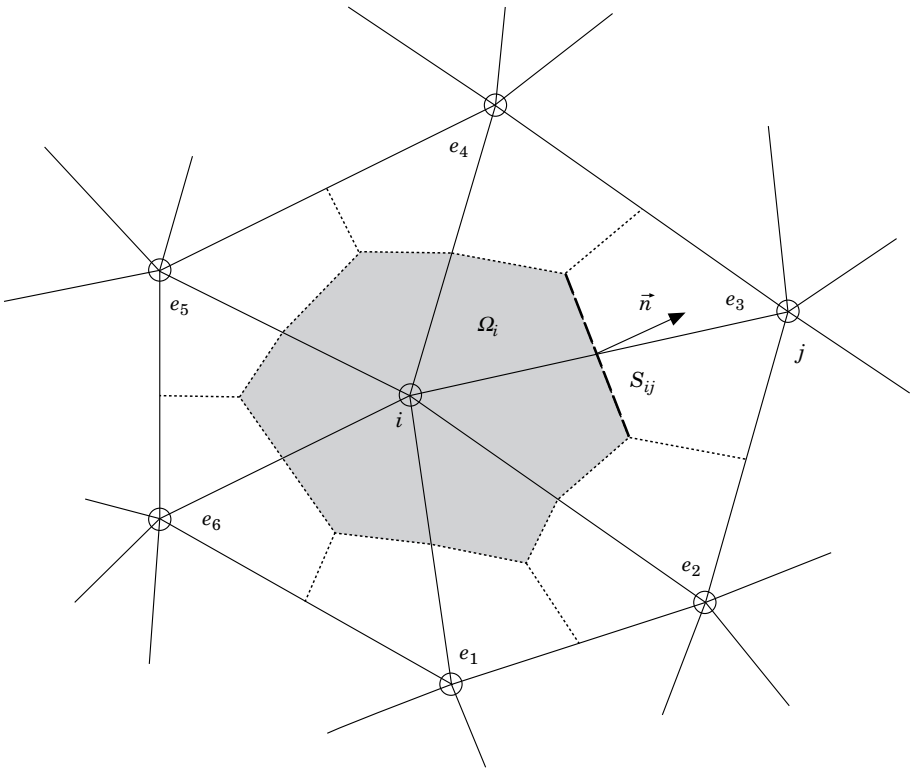

(a)

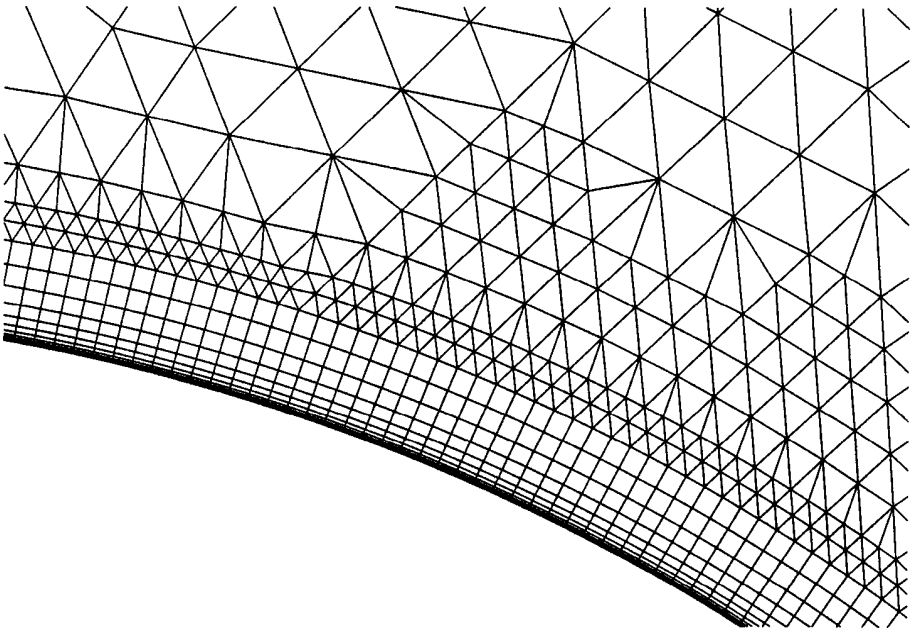

(b)

Figure 1. (a) Schematic representation of a control volume. (b) Structured-unstructured grid interface near the solid surface.

the thickness of the structured layer in the near-wall region: the size of control volumes in the region of the structured-unstructured grid interface should be almost the same, while between the structured and unstructured grid regions there are no overlapping control volumes.

2.2.1. *Unstructured grid region*

In the unstructured grid region a predictor-corrector scheme is applied for both the inviscid and viscous fluxes. In the predictor step no Riemann solver is employed, while the Roe scheme (Roe 1981) is used in the corrector step. According to Fursenko *et al.* (1995), in order to enhance the spatial accuracy a linear reconstruction of the primitive variables, $V = (\rho, u, v, p)^{\mathrm{T}}$, is used for all control volumes. The gradient $\partial V/\partial\alpha_i$ of the primitive variables on each control volume [Figure 1(a)] are calculated by the minimum value of the average gradient $\overline{\partial V}/\partial\alpha_i$ and the gradients $\partial V/\partial\alpha_e$ in the triangles (e) surrounding the node i:

$$\frac{\partial V}{\partial\alpha_i} = \min_e \left[\frac{\overline{\partial V}}{\partial\alpha_i}, 2\frac{\partial V}{\partial\alpha_e}\right], \qquad \alpha = x,y; \qquad \left(\frac{\overline{\partial V}}{\partial\alpha_i}\right) = \frac{1}{\Omega_i}\sum_e (\nabla V)_e \Omega_e \tag{2}$$

Using the above gradients, the primitive variables at the cell faces of the control volume are calculated as

$$V_{ij}^{\mathrm{in}} = V_i + 0{\cdot}5(\nabla V)_i \cdot (\vec{\mathbf{ij}}) \tag{3}$$

where $(\vec{\mathbf{ij}})$ is the vector between the nodes i and j. The predictor step calculates an intermediate value $\tilde{U}_i$ of the conservative variables as

$$\tilde{U}_i\Omega_i = U_i^n\Omega_i - \Delta t \sum_j \{[F_x^c(V_{ij}^{\mathrm{in}}) + F_x^v(V_{ij}^{\mathrm{in}})]n_x S_{ij} + [F_y^c(V_{ij}^{\mathrm{in}}) + F_y^v(V_{iy}^{\mathrm{in}})]n_y S_{ij}\} \tag{4}$$

where j denotes grid points surrounding the node i. Ω_i is the control volume around the node i and S_{ij} is the area of the interface between the volumes i and j [Figure 1(a)].

Then for each volume i the corrector step is performed:

$$U_i^{n+1}\Omega_i = U_i^n\Omega_i - \Delta t \sum_j \{[F_x^c(W_{ij}) + F_x^v(W_{ij})]n_x S_{ij} + [F_y^c(W_{ij}) + F_y^v(W_{ij})]n_y S_{ij}\} \tag{5}$$

where W_{ij} is the average value of the primitive variables obtained by the Roe scheme, considering that the left $(\tilde{V}_{ij}^{\mathrm{in}})$ and right $(\tilde{V}_{ij}^{\mathrm{out}})$ states of the Riemann problem are defined as

$$\tilde{V}_{ij}^{\mathrm{in}} = 0{\cdot}5[\tilde{V}_i + V_i + (\nabla V)_i \cdot (\vec{\mathbf{ij}})], \qquad \tilde{V}_{ij}^{\mathrm{out}} = 0{\cdot}5[\tilde{V}_j + V_j + (\nabla V)_j \cdot (\vec{\mathbf{ji}})] \tag{6}$$

The above predictor-corrector procedure (henceforth labelled as the $L(\Delta t)$ operator) is performed twice.

2.2.2. *Structured grid region*

In the structured grid region a more complicated procedure is followed in order to improve the efficiency of the unsteady calculations in the boundary layer and avoid significant reduction of the CFL number in the near-wall region. The above predictor-corrector scheme, $L(\Delta t)$, is also applied to the inviscid fluxes in the tangential to the body direction using a time step Δt (always smaller or equal to the physical one) defined as

$$\Delta t = \min(\Delta t_1, \Delta t_2) \tag{7}$$

where Δt_1 and Δt_2 are defined by

$$\Delta t_1 = \frac{\mathrm{CFL}}{\sqrt{2}} \frac{\Delta I}{(|\mathbf{v}| + c)\left(1 + 2\dfrac{\rho \Delta l (|\mathbf{v}| + c)}{\mu \max(1, \gamma/\mathrm{Pr})\mathrm{Re}}\right)} \tag{8}$$

$$\Delta t_2 = \frac{\mathrm{CFL} \cdot \Delta l}{|\vec{v}| + c} \tag{9}$$

where Δl is a characteristic length of the cell, c is the speed of sound, γ is the ratio of specific heats and Re is the Reynolds number.

The above procedure is labelled as $L_1(\Delta t)$. The same procedure is also applied to the inviscid flux in the normal direction performing m subiterations and using a time step $\Delta t/m$. This procedure is labelled as $L_2(\Delta t/m)$.

For the viscous fluxes the predictor-corrector procedure, labelled as $L^v(\Delta t)$, is written as follows:

- Predictor

$$U_{i,j}^{n+1/2} = U_{i,j}^n - \frac{\Delta t}{\Omega_{i,j}} \sum F_{(v),o}^n \tag{10}$$

- Corrector

$$U_{i,j}^{n+1} = U_{i,j}^n - 0{\cdot}5 \frac{\Delta t}{\Omega_{i,j}} \left[\sum F_{(v),o}^n + \sum F_{(v),0}^{n+1/2}\right] - 0{\cdot}5 \frac{\Delta t}{\Omega_{i,j}} \left[\sum F_{(v),m}^n + \sum F_{(v),m}^{n+1}\right] \tag{11}$$

where the sum is obtained for all faces of the quadrilateral elements. The viscous flux $F_{(v),m}$ contains the second order derivatives in the normal direction, and the flux $F_{(v),o}$ contains the rest of the viscous terms. The development of equation (11) results in a block tridiagonal matrix of coefficients, which is solved by the Thomas algorithm. The predictor-corrector procedure described above for the structured grid region is performed twice at each time step. By making use of the symbolic operators $L_1(\Delta t)$, $L_2(\Delta t/m)$ and $L^v(\Delta t)$ this procedure is represented as

$$L(\Delta t) = L_1^c(\Delta t)\left[L_2^c\left(\frac{\Delta t}{m}\right)\right]^m L^v(\Delta t) \times L^v(\Delta t)\left[L_2^c\left(\frac{\Delta t}{m}\right)\right]^m L_1^c(\Delta t) \tag{12}$$

2.3. Grid Adaptation

The local adaptation of the unstructured grid during the numerical solution provides a powerful tool for the accurate simulation of non-stationary, gas-dynamic phenomena. The adaptation algorithm in the present paper is similar to that developed by Löhner (1987). The refinement/coarsening criterion is based on second-order differences of density (Fursenko *et al.* 1995):

$$E_i = \max_e \left(\frac{|(\nabla\rho)_e - \overline{(\nabla\rho)_i}|}{|(\nabla\rho)_e| + |\overline{(\nabla\rho)_i}| + \varepsilon\,|\rho_i|\,d^{-1}}\right) \tag{13}$$

where e denotes the neighbouring triangles of the node i [Figure 1(a)]. The parameter d represents a characteristic size of the cell, and ε is a filter coefficient which has to be properly chosen to enhance grid adaptation. The grid is coarsened or refined by comparing the value of E_i at each node with the coarsening (T_c) and refining (T_r) criteria which are prescribed as input values in the computational code. If $E_i > T_r$, all triangles of vertex i will be refined, while if $E_i < T_c$ the node i may be removed.

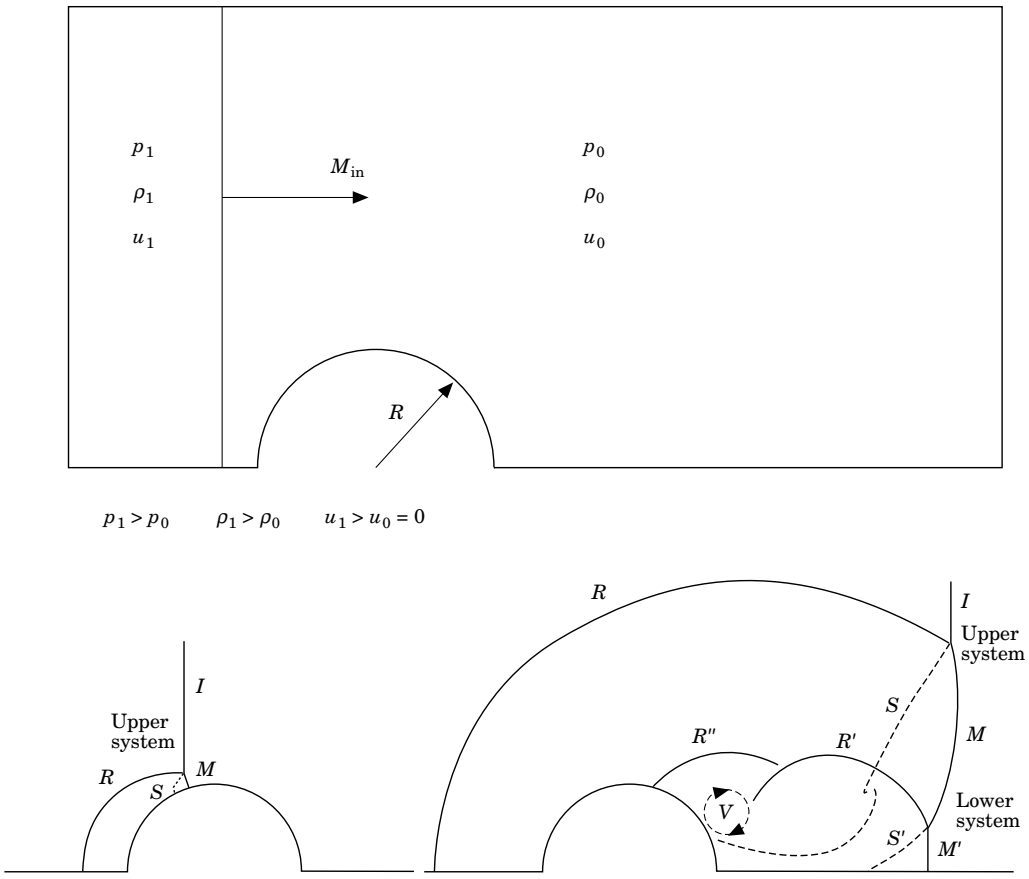

Figure 2. Initial conditions for the shock-cylinder interaction and main flow features: upper and lower shock-wave systems.

3. RESULTS

3.1. Validation Against Experimental Results

The numerical method was initially validated against experimental data for the shock-wave propagation over a cylinder. A schematic representation of the flow geometry including the most important flow features is shown in Figure 2. The upper and lower shock-wave systems are discussed later. Experimental measurements of the pressure and skin friction in such flows are rare. Takayama *et al.* (1985) have performed shock tube measurements and calculations, based on structured-grids, for the pressure and drag coefficient during the diffraction of shock waves over a cylinder. Comparison of the present computations with the Takayama *et al.* (1985) experimental results is shown in Figure 3. In these figures the dimensionless time, t_r, is defined as

$$t_r = tu_{\text{in}}/R \tag{14}$$

where t, R and u_{in} are the time, radius of the cylinder and velocity of the incident shock, respectively. The computations have been performed at $M_{\text{in}} = 1{\cdot}3$ and $M_{\text{in}} = 2{\cdot}6$, and at Reynolds number $\text{Re} = 7 \times 10^5$. In Figure 3 Takayama's calculations for the drag coefficient history are also included, revealing that the present computations are in closer agreement with the experiment. These results were obtained using five

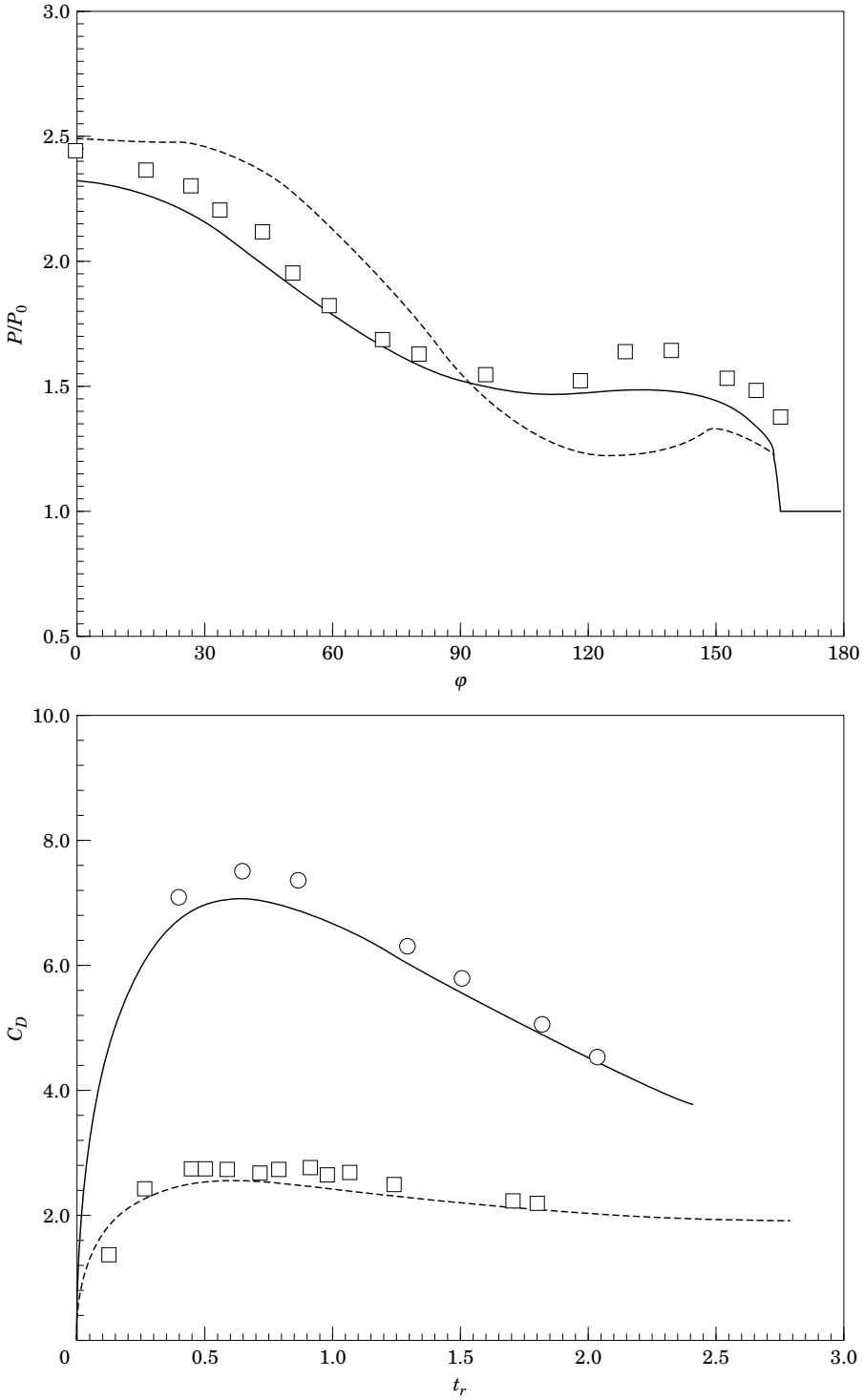

Figure 3. Comparison of the pressure load (P/P_o) and drag coefficient (C_D) history with the experimental and numerical results by Takayama *et al.* (1985). (a) P/P_0 results for $M_{in} = 1{\cdot}3$, $Re = 7 \times 10^6$, $t_r = 2{\cdot}4$: (□) experiment (Takayama *et al.* (1985); (– – –) calculation (Takayama *et al.* 1985); (——) present results. (b) C_D results for $Re = 7 \times 10^5$: (○) experiment by Takayama *et al.* for $M_{in} = 1{\cdot}3$; (□) for $M_{in} = 2{\cdot}6$; (——) present results for $M_{in} = 1{\cdot}3$; (– – –) for $M_{in} = 2{\cdot}6$.

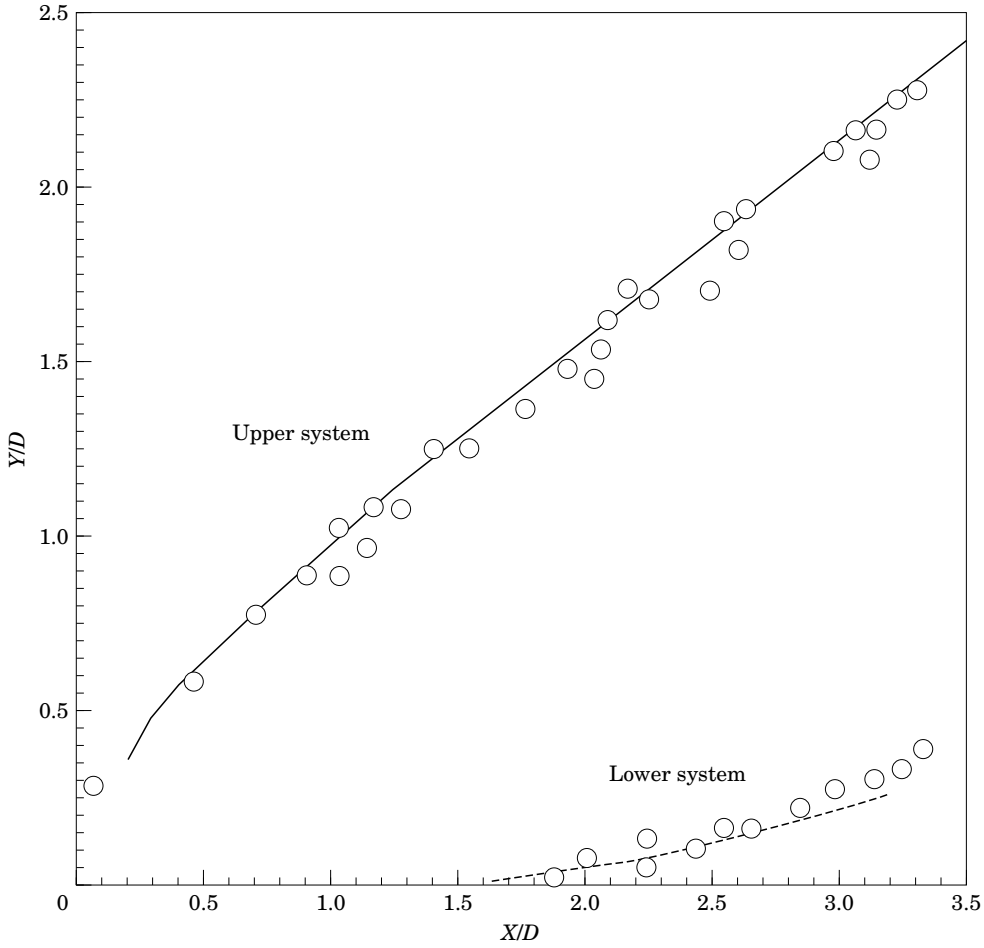

Figure 4. Navier-Stokes results for the triple-point path at $M_{in} = 2{\cdot}81$ and comparison with the experimental results by Bryson & Gross (1961). (○) Experiment (Bryson & Gross 1961); (—) present results; (– – –) present results.

adaptation levels. Computations using more adaptation levels (i.e. a finer grid) showed that the pressure and drag coefficients remained unchanged. Hence the above results are the grid-independent solution. As a second test, the triple-point path of the upper and lower shock-wave systems at $M_{in} = 2{\cdot}81$ was computed and compared with the experimental results by Bryson & Gross (1961). A schematic representation of the triple-point on the upper and lower shock-wave systems is shown in Figure 2. In Figure 4 the comparison shows that the computations are in statisfactory agreement with the experiment.

3.2. Viscous Simulations at Various Mach Numbers

The shock-cylinder interaction was studied at incident-shock Mach numbers $M_{in} = 1{\cdot}7$, 3 and 5. The Reynolds number was $\mathrm{Re} = 2{\cdot}5 \times 10^5$ and the ratio of specific heats $\gamma = 1{\cdot}4$. However, in order to examine the importance of the viscous effects in such flows, Euler calculations were also carried out, and these are discussed later. The collision of the shock wave with the cylinder at various time instants is shown in

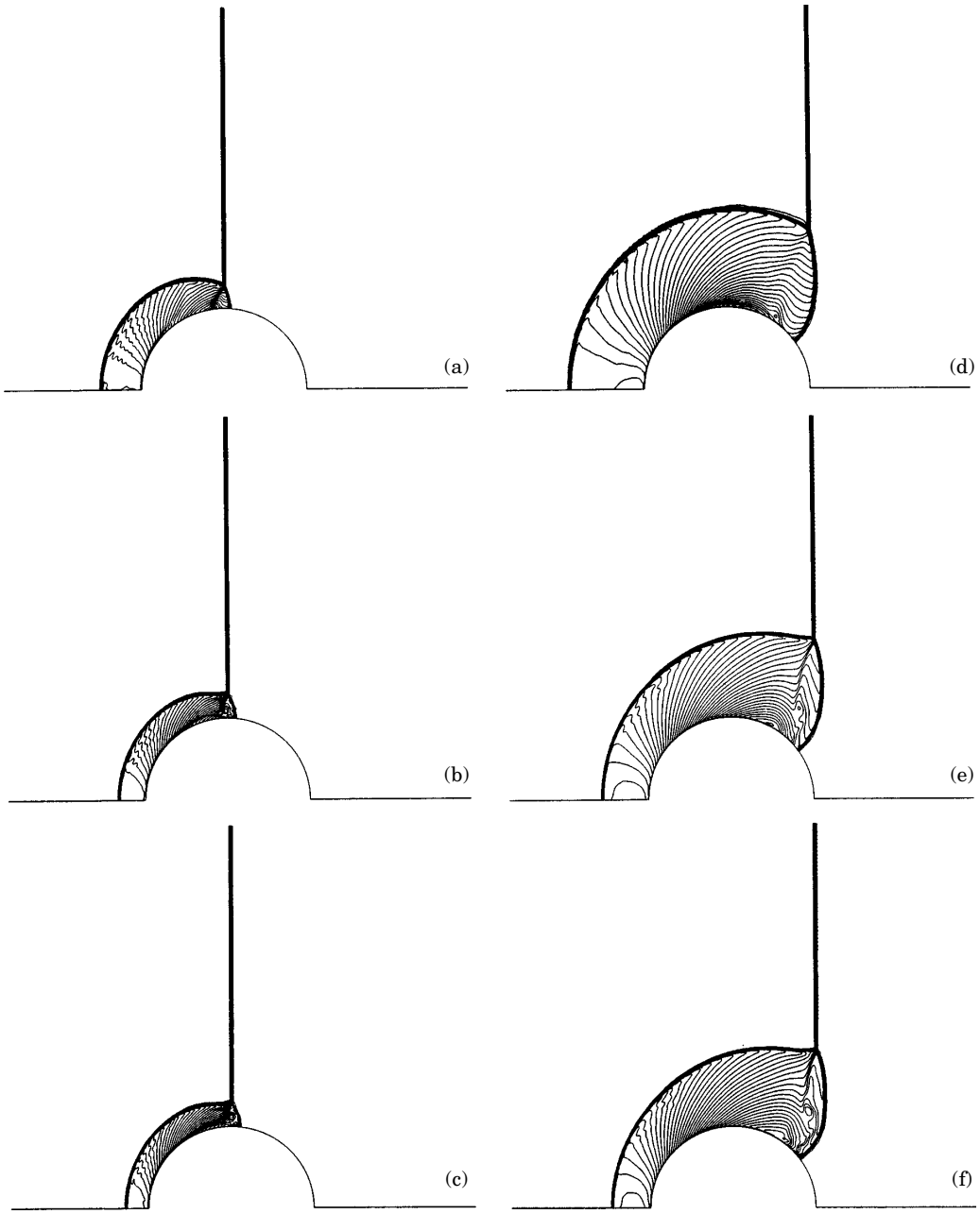

Figure 5. Isodensity lines (Navier-Stokes calculations) at $t_r = 1$: (a) $M_{in} = 1{\cdot}7$, (b) $M_{in} = 3$ and (c) $M_{in} = 5$; and at $t_r = 2$: (d) $M_{in} = 1{\cdot}7$, (e) $M_{in} = 3$ and (f) $M_{in} = 5$.

Figures 5–9 by plotting the density contours. Density contours are presented at Mach numbers $M_{in} = 1{\cdot}7$, 3 and 5. After the initial collision of the shock wave with the cylinder, a regular shock reflection occurs which is followed by a Mach-reflection (Figure 5). This is the upper-shock wave system and consists of the incident shock (I), the reflected shock (R), the Mach stem (M) and the slip surface (S). A schematic representation of these phenomena is also shown in Figure 2. An enlargement of the region around the intersection of the three shock waves (triple-point), in the upper

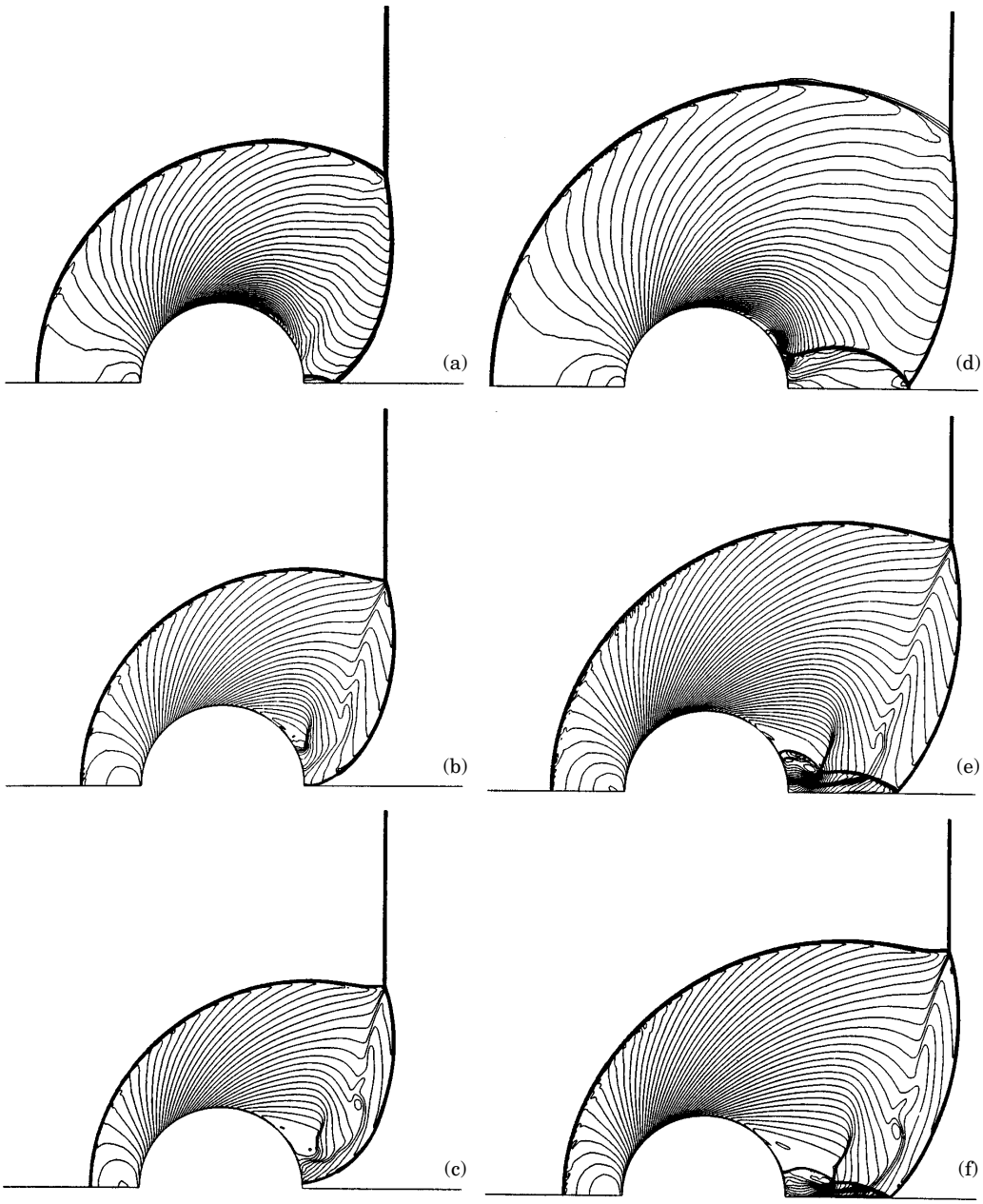

Figure 6. Isodensity lines (Navier-Stokes calculations) at $t_r = 3$: (a) $M_{in} = 1{\cdot}7$, (b) $M_{in} = 3$ and (c) $M_{in} = 5$; and at $t_r = 4$: (d) $M_{in} = 1{\cdot}7$, (e) $M_{in} = 3$ and (f) $M_{in} = 5$.

system, is shown in Figure 10. Behind the Mach stem a vortex appears which moves away from the solid surface when increasing the Mach number [Figures 10(a,b,c)]. At $M_{in} = 1{\cdot}7$ a single Mach reflection occurs [Figure 10(a)] which turns into transitional Mach reflection at $M_{in} = 5$ [Figure 10(c)]. This is similar to the gas-dynamic phenomena observed during the interaction of shock waves over a wedge (Glass & Sislian 1994). Later, the upper shock wave system moves downstream and grows towards the upper boundary, while the Mach stem becomes more curved (Figures 5 and 6). At the same

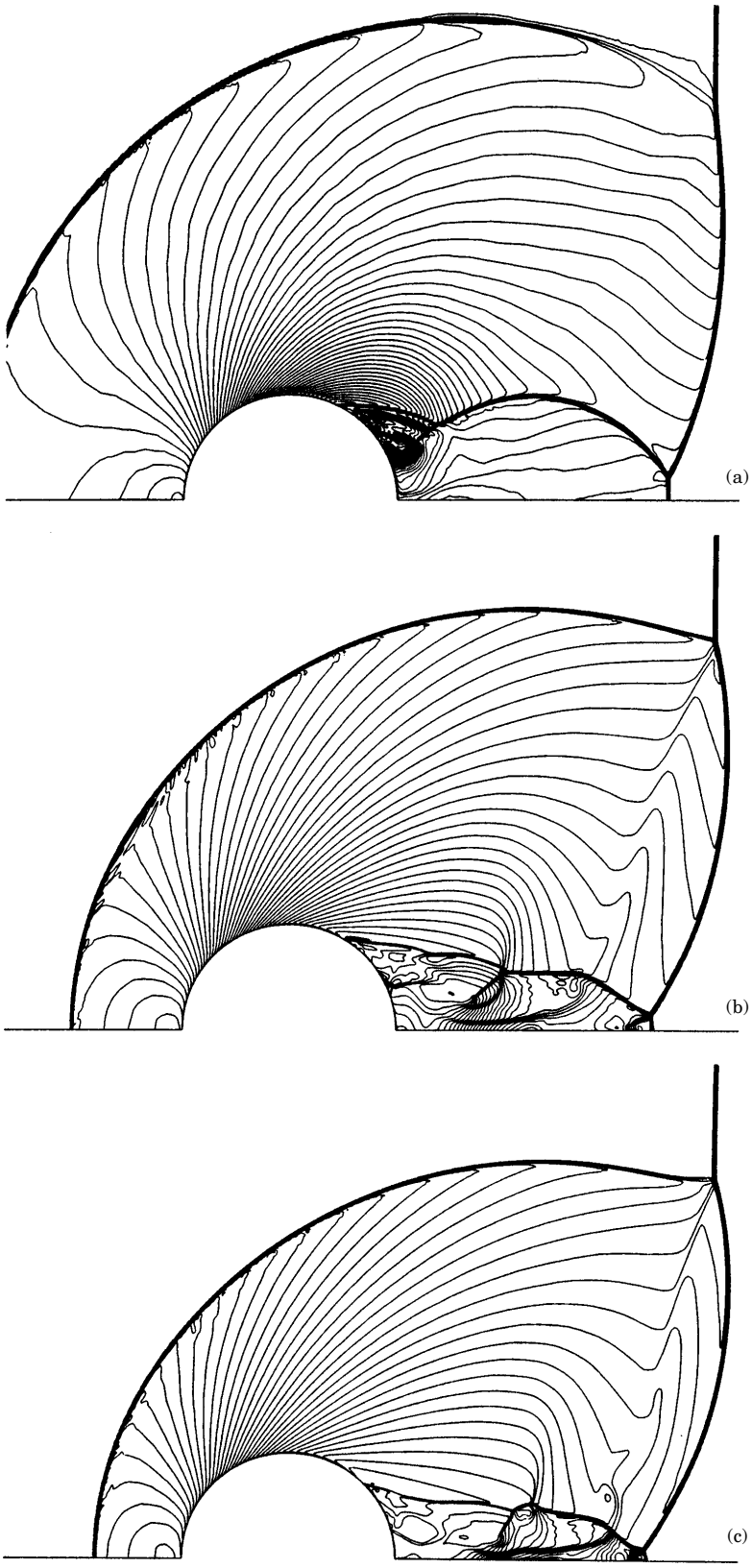

Figure 7. Isodensity lines (Navier-Stokes calculations) at $t_r = 5$: (a) $M_{in} = 1{\cdot}7$, (b) $M_{in} = 3$ and (c) $M_{in} = 5$.

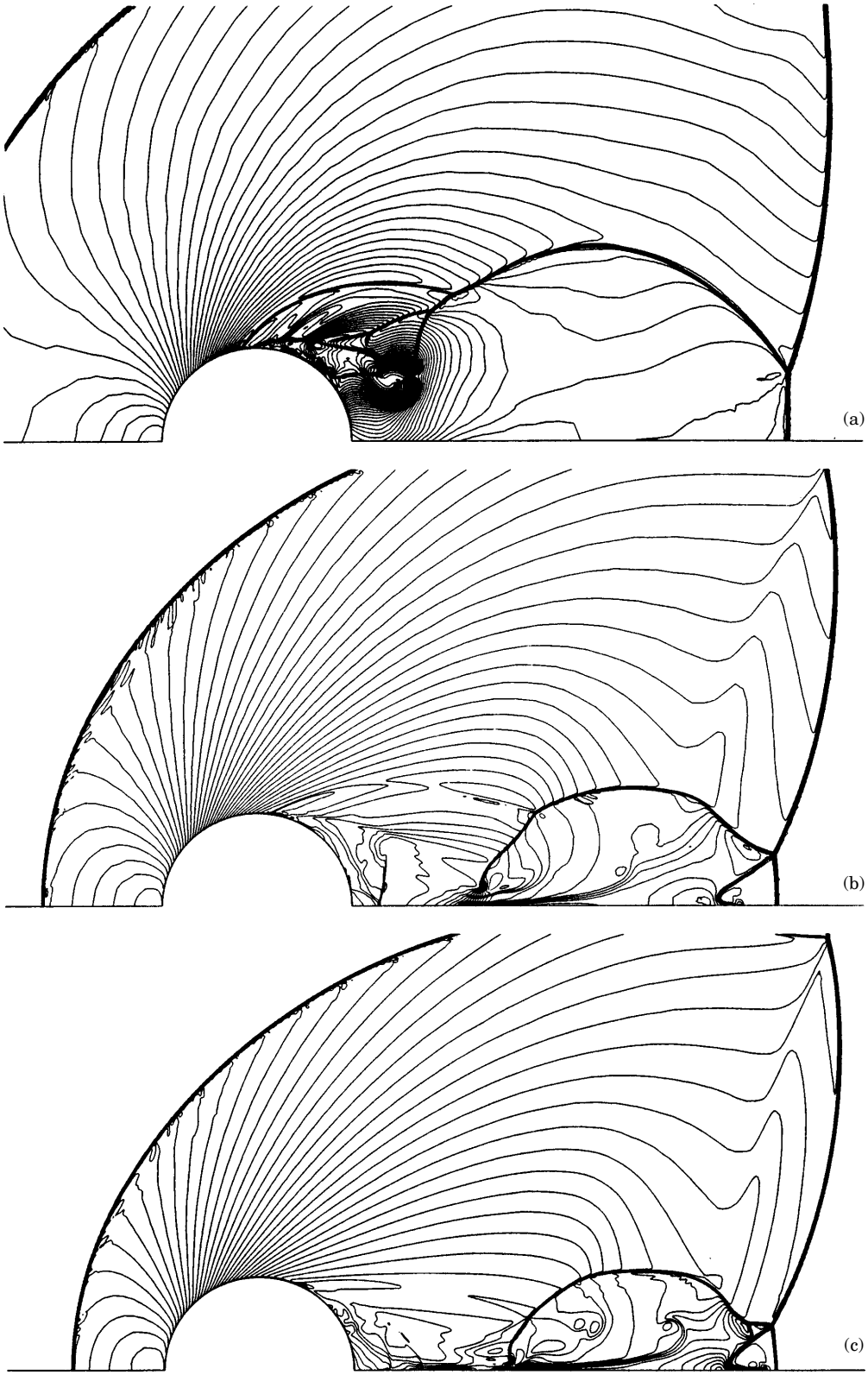

Figure 8. Isodensity lines (Navier-Stokes calculations) at $t_r = 7$: (a) $M_{in} = 1{\cdot}7$, (b) $M_{in} = 3$ and (c) $M_{in} = 5$.

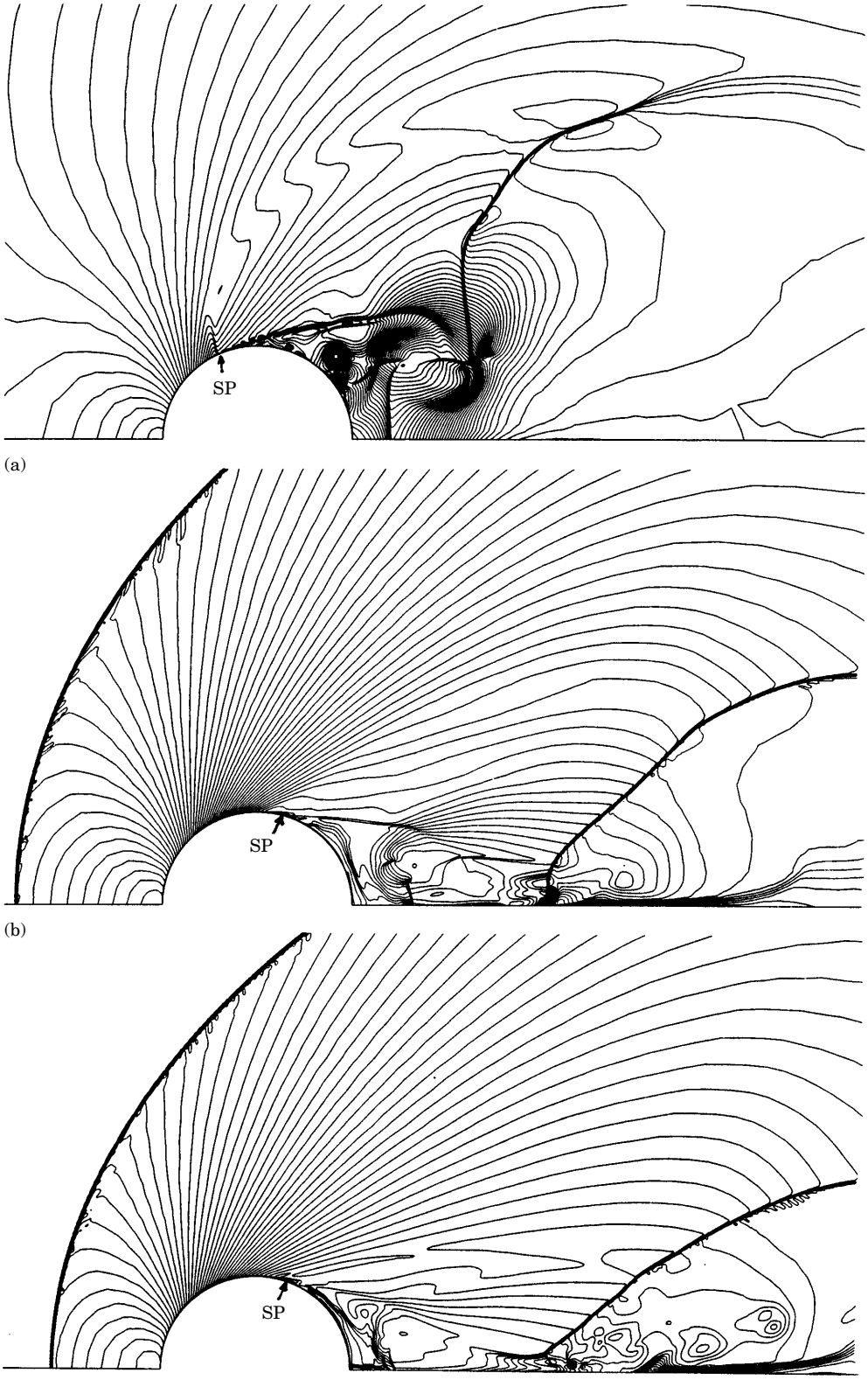

Figure 9. Isodensity lines (Navier-Stokes calculations) at $t_r = 10$: (a) $M_{in} = 1{\cdot}7$, (b) $M_{in} = 3$ and (c) $M_{in} = 5$. (SP is the separation point).

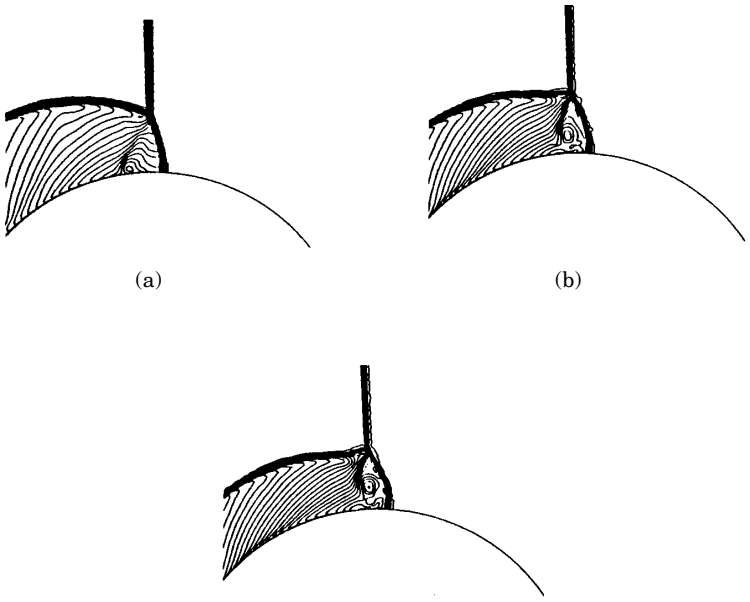

Figure 10. Enlargement of the region around the triple-point of the upper shock wave system at $t_r = 1$: (a) $M_{in} = 1{\cdot}7$, (b) $M_{in} = 3$, and (c) $M_{in} = 5$; (Navier-Stokes calculations).

time a compression wave behind the Mach stem (Figure 5) appears for all Mach numbers, but it turns into a shock wave only at $M_{in} = 3$ and 5 (Figure 6).

After the shock system passes the cylinder, the Mach stem is reflected behind the plane of symmetry (Figures 6 and 7). The present results reveal that the onset of this reflection depends on the incident-shock Mach number and appears earlier when M_{in} is smaller (Fig. 6). This reflection is initially regular and becomes single, transitional or double Mach reflection depending on the incident-shock Mach number (Figures 7 and 8). The new shock wave system behind the cylinder is called the lower system (Figure 2) and consists of the shock wave (M) (this is due to the Mach stem of the upper system), the reflected shock wave (R'), the Mach stem (M',) and the slip surface (S') (Figure 2). The reflected shock wave (R') interacts with the separated boundary layer behind the cylinder, while a second shock wave (R'') appears between the cylinder and the reflected shock R' of the lower system. This is schematically shown in Figure 2. As the Mach number increases, the point of intersection of the shock waves R' and R'' moves downstream (Figures 6 and 7). During the development of R'', additional vortices and shock structures arise behind the cylinder, especially at $M_{in} = 1{\cdot}7$ (Figures 8 and 9).

3.3. Comparison Between Euler and Navier-Stokes Calculations

Euler calculations were performed at Mach numbers $M_{in} = 1{\cdot}7$, 3 and 5. The isodensity contours are shown in Figures 11, 12 and 13 for the time instants $t_r = 2$, 4 and 10, respectively. These results are compared with the corresponding contours shown in Figures 5, 6 and 9, respectively. At $t_r = 2$ the Euler and Navier-Stokes solutions are very similar (Figures 5 and 11). At $t_r = 4$ (Figures 6 and 12) the differences are larger for all Mach numbers. At $M_{in} = 1{\cdot}7$ the viscous calculation reveals a λ-shock at $\phi \approx 160°$. At higher Mach numbers ($M_{in} = 3$, 5) the Navier-Stokes calculations reveal that the shock structure, close to $\phi = 180°$, is influenced by the interaction with the

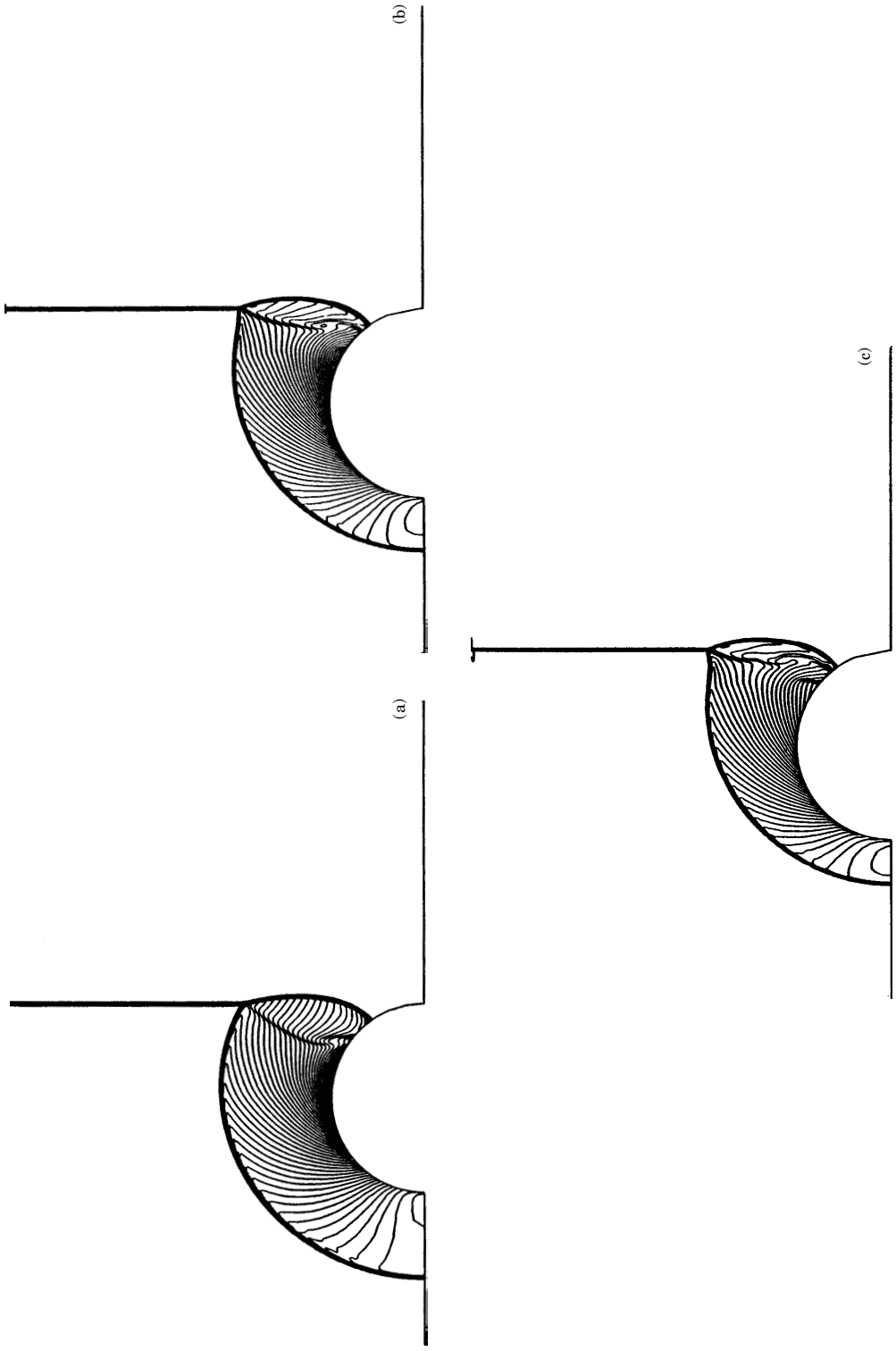

Figure 11. Isodensity lines (Euler calculations) at $t_r = 2$: (a) $M_{in} = 1{\cdot}7$, (b) $M_{in} = 3$ and (c) $M_{in} = 5$.

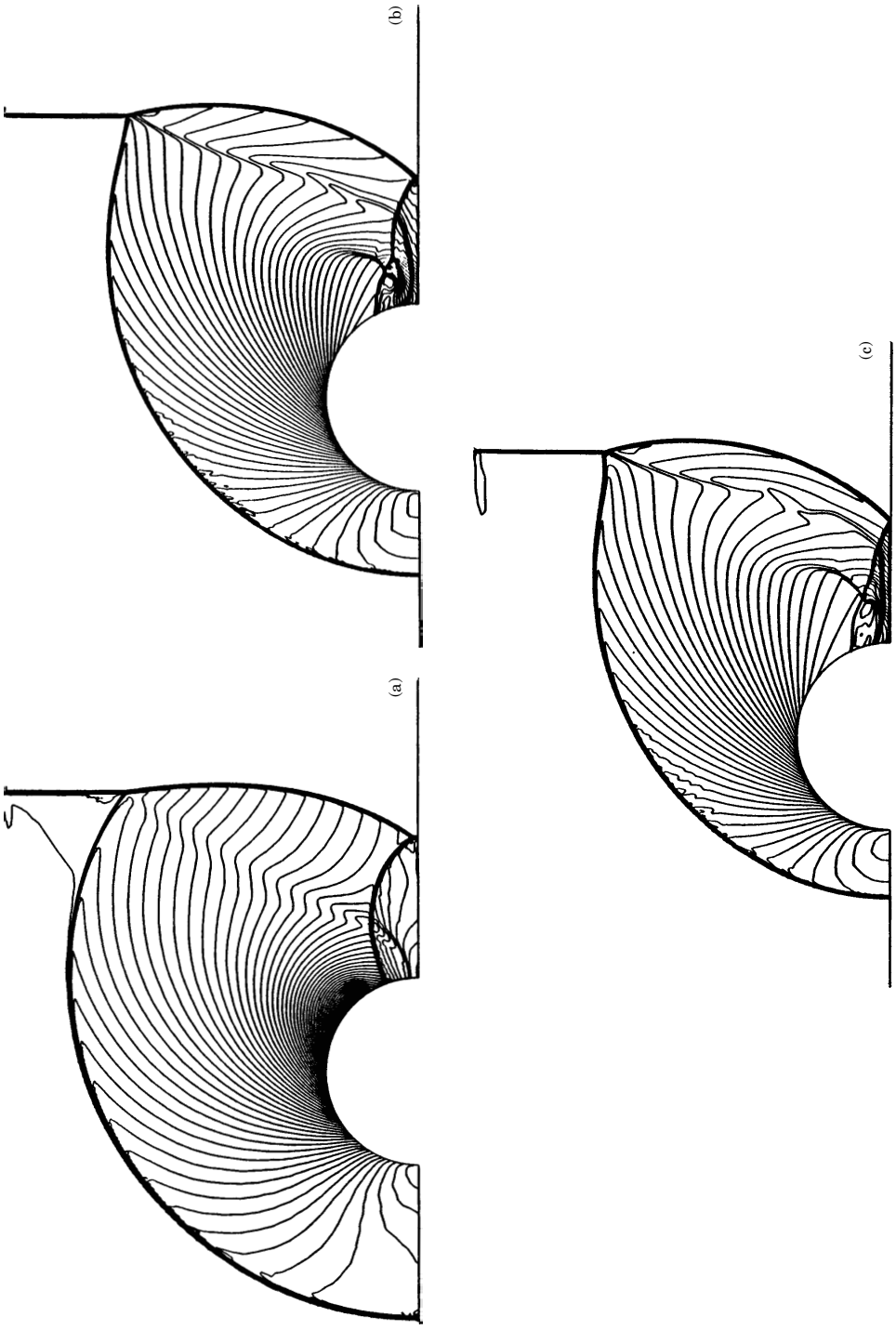
(b)
(c)
(a)

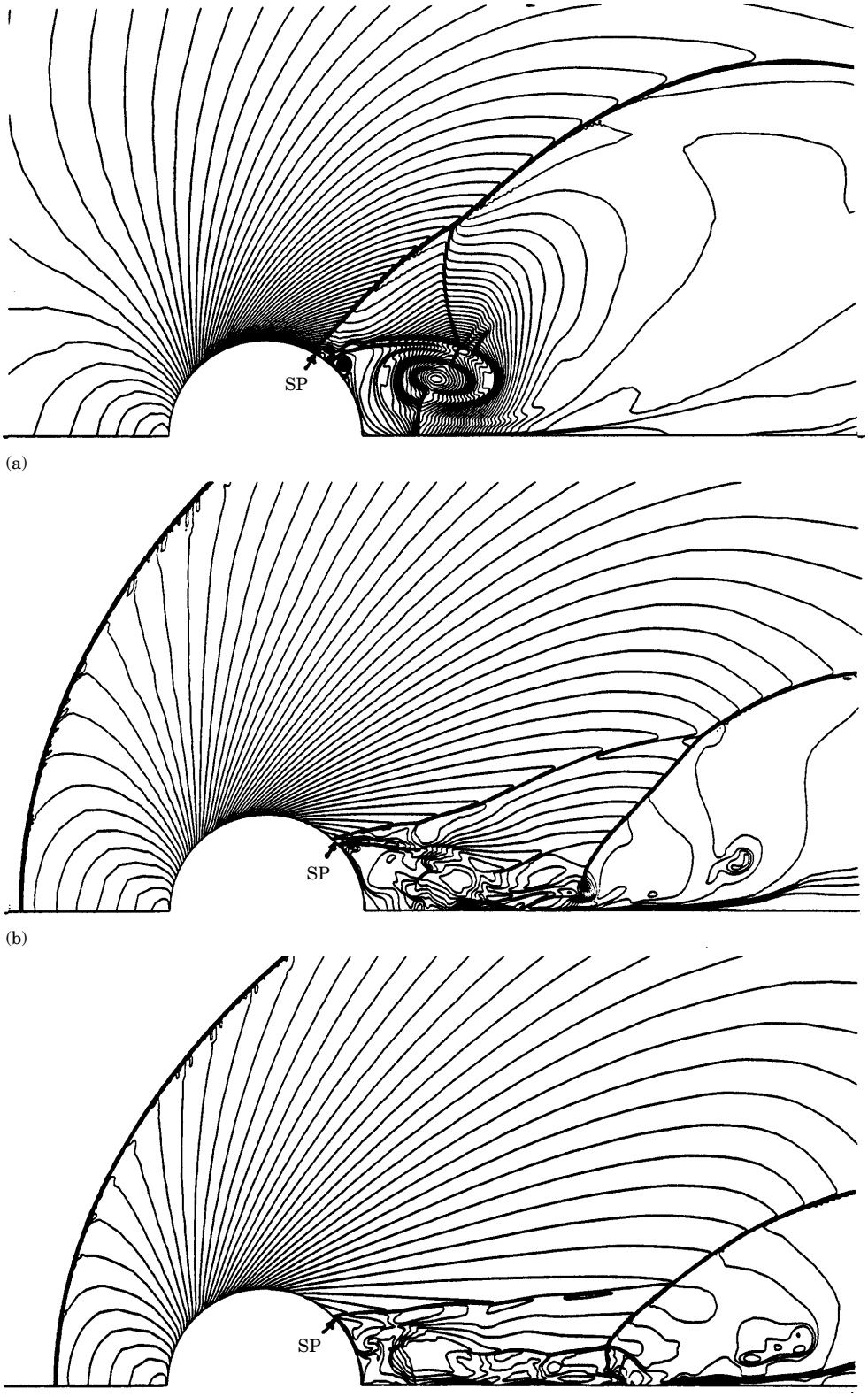

Figure 13. Isodensity lines (Euler calculations) at $t_r = 10$: (a) $M_{in} = 1{\cdot}7$, (b) $M_{in} = 3$ and (c) $M_{in} = 5$.

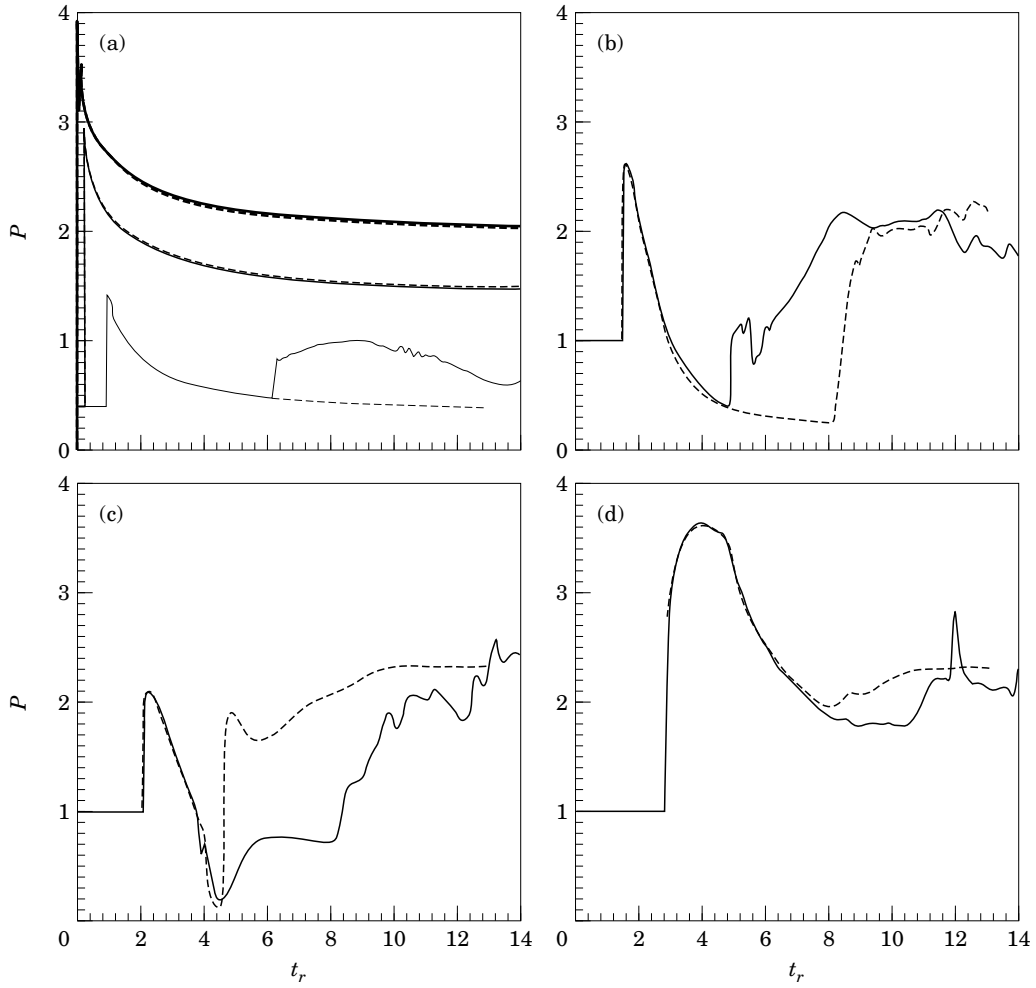

Figure 14. Pressure load histories (Euler and Navier-Stokes calculations) at $M_{in} = 1{\cdot}7$. (a) Viscous: (——) $\phi = 0°$, (——) $\phi = 40°$, (——) $\phi = 90°$; inviscid: (— — —) $\phi = 0°$, (— — —) $\phi = 40°$, (— — —) $\phi = 90°$. (b) $\phi = 120°$: (——) viscous, (– – –) inviscid. (c) $\phi = 150°$: (——) viscous, (– – –) inviscid. (d) $\phi = 180°$: (——) viscous, (– – –) inviscid.

boundary layer. Finally, the differences between Euler and Navier-Stokes calculations are larger at $t_r = 10$ (Figures 9 and 13). The viscous calculations reveal that diffusion plays an important role in the wake, particularly near the cylinder surface. The Euler solutions provide an unrealistic picture of the flow field, especially regarding the onset of flow separation (SP point in Figures 9 and 13). For not very long time intervals (e.g., $t_r < 10$) transition from laminar to turbulent flow has not been observed experimentally (Syshchikova *et al.* 1967; Takayama *et al.* 1985). Calculations for $t_r > 10$ were not carried out because it is an open question whether the assumption of laminar flow is still valid in the wake of the flow for very long time intervals. Moreover, the authors are not aware of any experimental investigation on this problem. On the other hand, calculations of the turbulent wake should preferably be done by large-eddy or direct numerical simulation, and certainly the computing requirements impose severe limitations in this case. Alternatively, one- or two-equation eddy-viscosity models could also be used, but the physical interpretation of the results is more difficult in this case

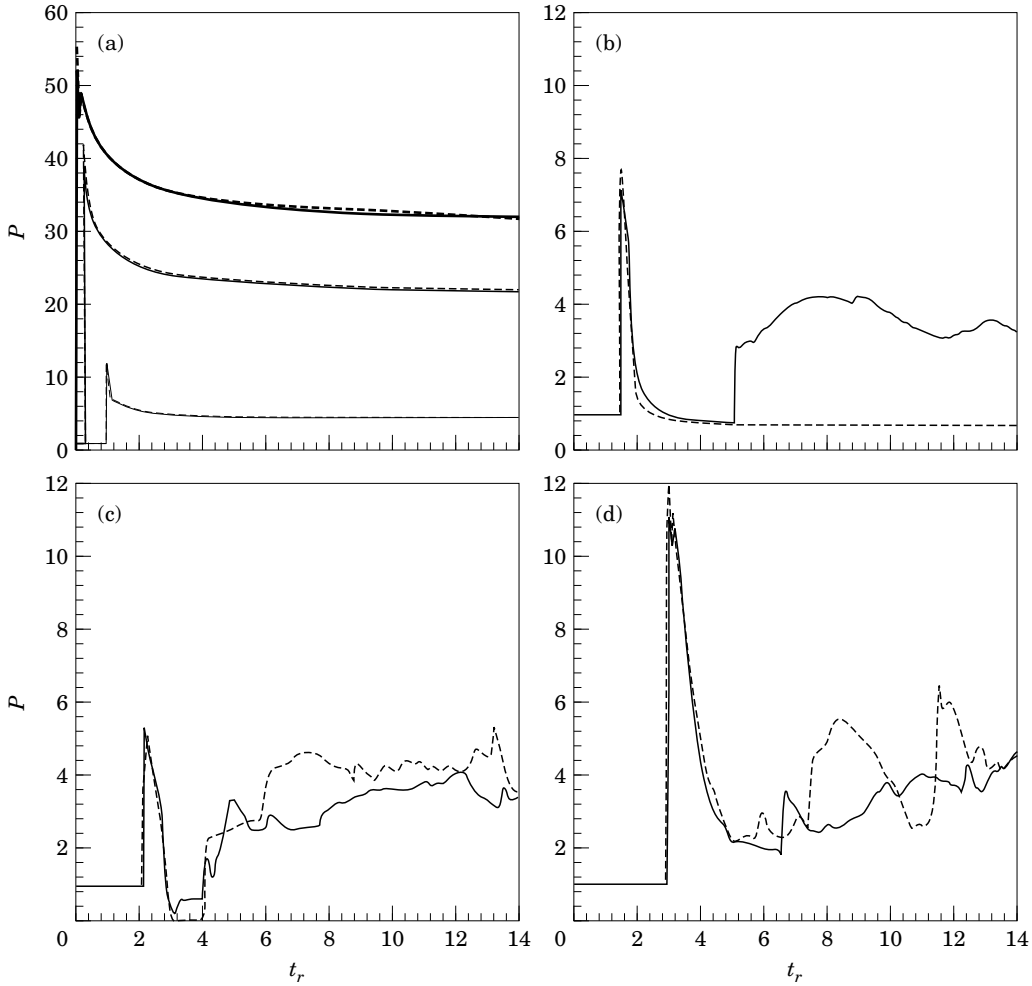

Figure 15. Pressure load histories (Euler and Navier-Stokes calculations) at $M_{in} = 3$. (a) Viscous: (—) $\phi = 0°$, (—) $\phi = 40°$, (—) $\phi = 90°$; inviscid: (— — —) $\phi = 0°$; (— — —) $\phi = 40°$, (– – –) $\phi = 90°$. (b) $\phi = 120°$: (—) viscous, (– – –) inviscid. (c) $\phi = 150°$: (—) viscous, (– – –) inviscid. (d) $\phi = 180°$: (—) viscous, (– – –) inviscid.

due to the assumptions introduced by these models. Study of interaction of strong shocks with turbulence is beyond the scope of the present work.

The pressure histories at several positions around the cylinder and for various incident-shock Mach numbers are shown in Figures 14–16. In these figures comparison between the inviscid and viscous results is also presented. The results reveal that most of the differences between inviscid and viscous calculations exist for $\phi \geq 90°$ and at time instants $t_r > 3{\cdot}5$. Higher pressure loads appear at higher Mach numbers, as expected, while both the inviscid and viscous solutions provide the same peak pressure in the first half of the cylinder ($\phi = 0°$–$90°$). It is also seen that for $\phi \leq 90°$ the pressure asymptotically reaches a constant value. The pressure histories at different positions in the second half of the cylinder reveal large variations, which are due to the vortices and shocks appearing in the wake near the cylinder surface.

The skin friction $c_f = \tau_w/(2\rho u_1^2)$ at different time instants and incident-shock Mach numbers is shown in Figure 17. The results reveal that at $M_{in} = 3$ and 5 the skin friction in the second half of the cylinder reaches an almost constant value closer to zero (e.g.

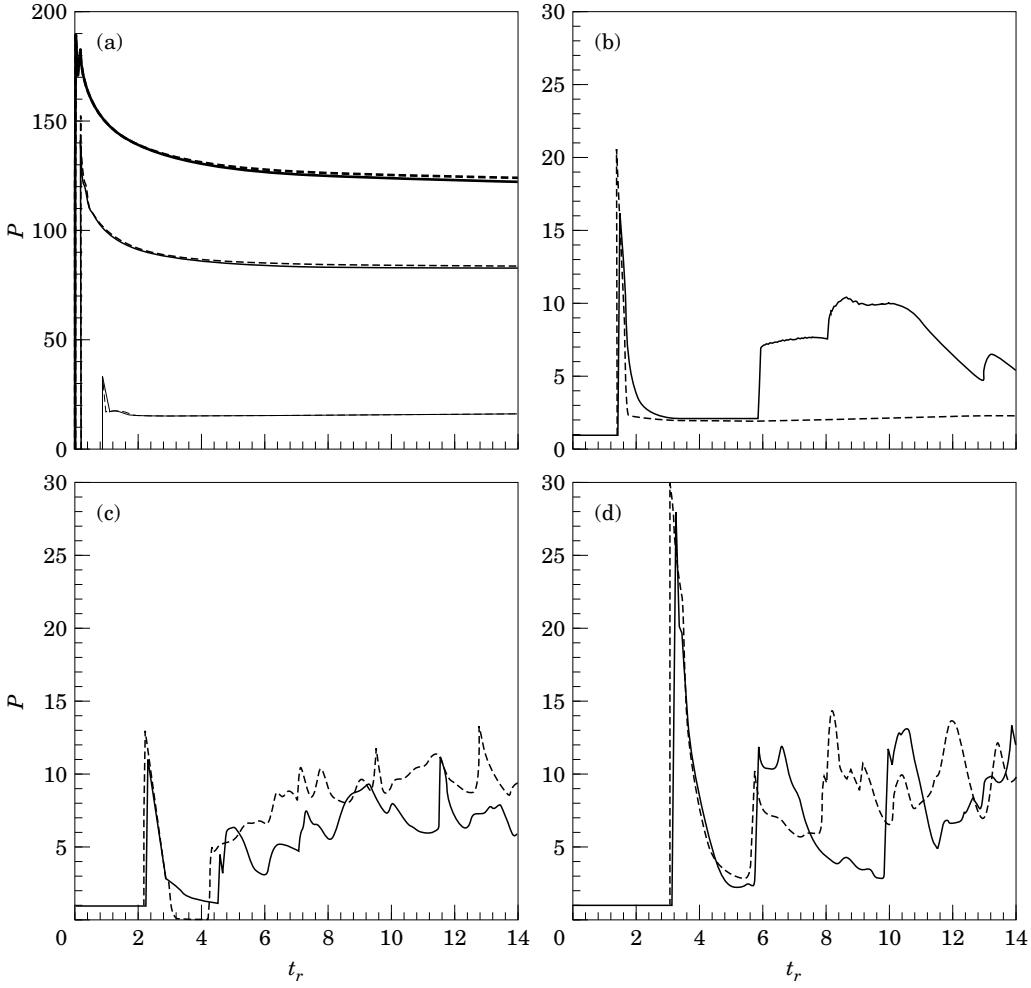

Figure 16. Pressure load histories (Euler and Navier-Stokes calculations) at $M_{in} = 5$. (a) Viscous: (—) $\phi = 0°$, (—) $\phi = 40°$; (—) $\phi = 90°$; inviscid: (— — —) $\phi = 0°$; (— — —) $\phi = 40°$; (– – –) $\phi = 90°$. (b) $\phi = 120°$: (—) viscous, (– – –) inviscid. (c) $\phi = 150°$: (—) viscous, (– – –) inviscid. (d) $\phi = 180$: (—) viscous, (– – –) inviscid.

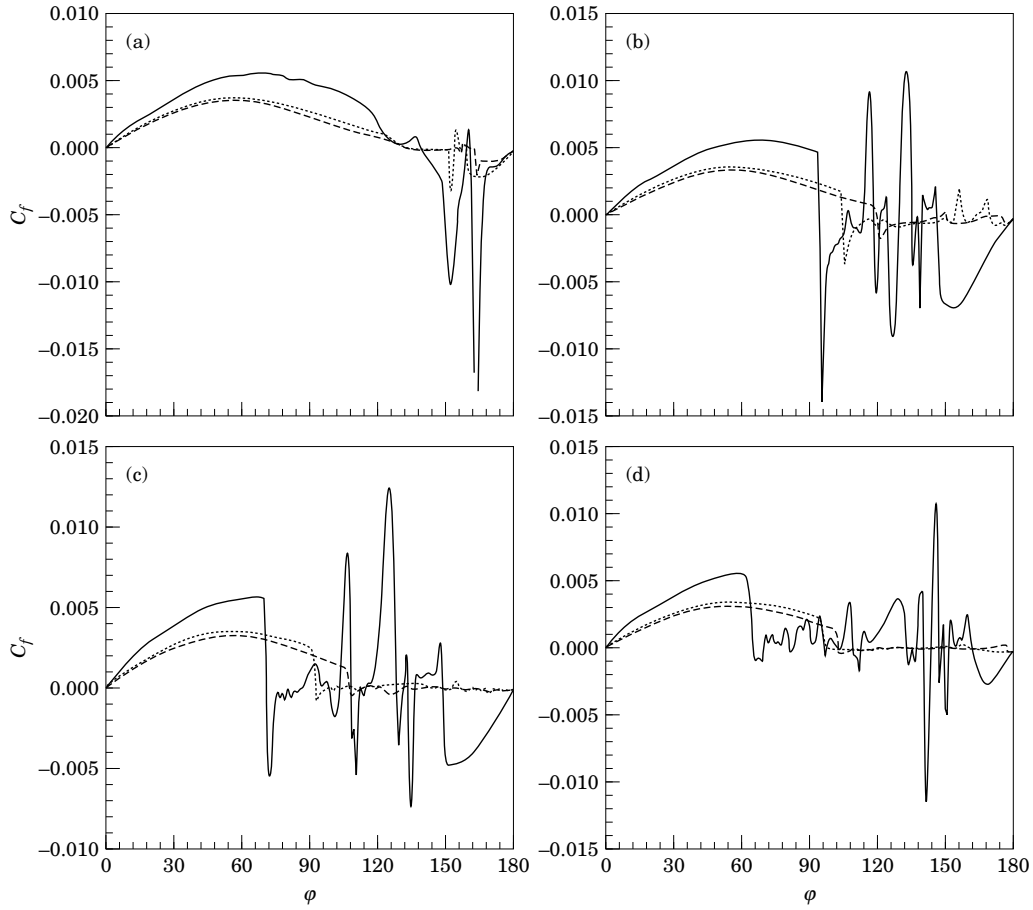

Figure 17. Skin-friction distribution at different time instants and Mach numbers. (a) $t_r = 4{\cdot}0$: (—) $M_{\text{in}} = 1{\cdot}7$, (· · ·) $M_{\text{in}} = 3{\cdot}0$, (– – –) $M_{\text{in}} = 5{\cdot}0$. (b) $t_{\text{r}} = 6{\cdot}0$: (—) $M_{\text{in}} = 1{\cdot}7$, (· · ·) $M_{\text{in}} = 3{\cdot}0$, (– – –) $M_{\text{in}} = 5{\cdot}0$. (c) $t_r = 8{\cdot}0$: (—) $M_{\text{in}} = 1{\cdot}7$, (· · ·) $M_{\text{in}} = 3{\cdot}0$, (– – –) $M_{\text{in}} = 5{\cdot}0$. (d) $t_r = 10{\cdot}0$: (—) $M_{\text{in}} = 1{\cdot}7$, (· · ·) $M_{\text{in}} = 3{\cdot}0$, (– – –) $M_{\text{in}} = 5{\cdot}0$.

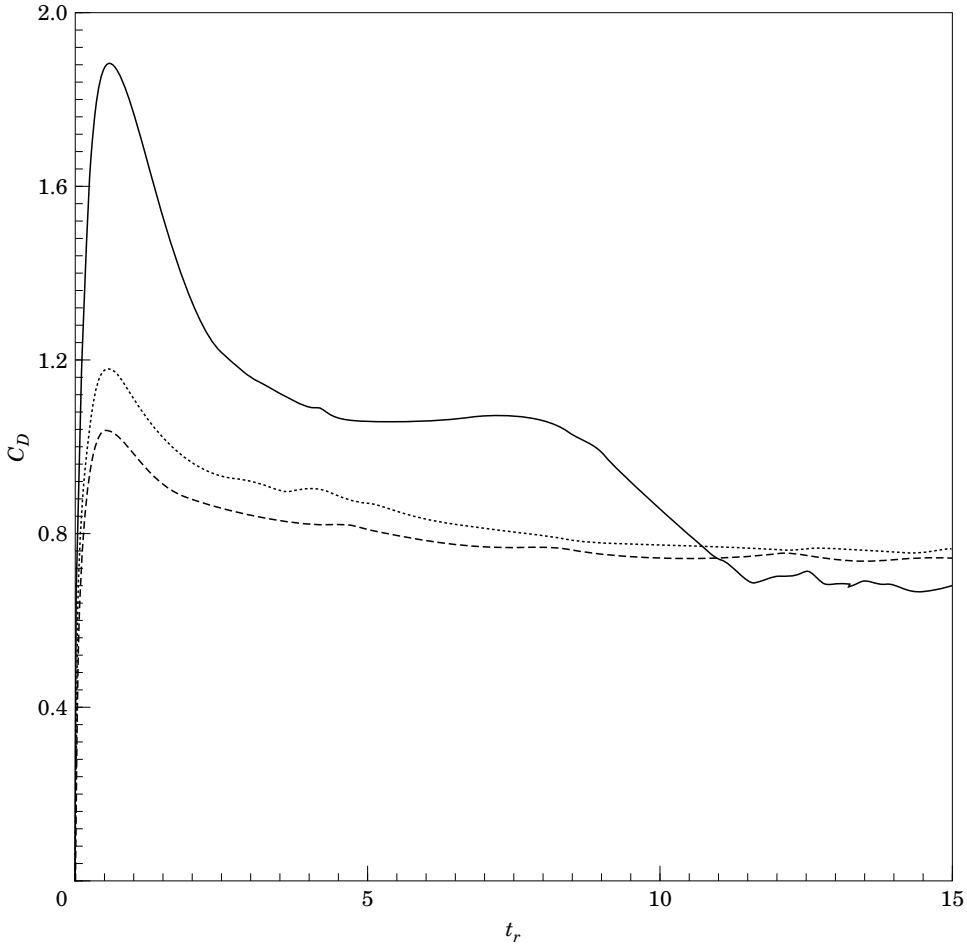

Figure 18. Drag coefficient histories at different incident-shock Mach numbers. (—) $M_{in} = 1{\cdot}7$; (· · ·) $M_{in} = 3{\cdot}0$; (– – –) $M_{in} = 5{\cdot}0$.

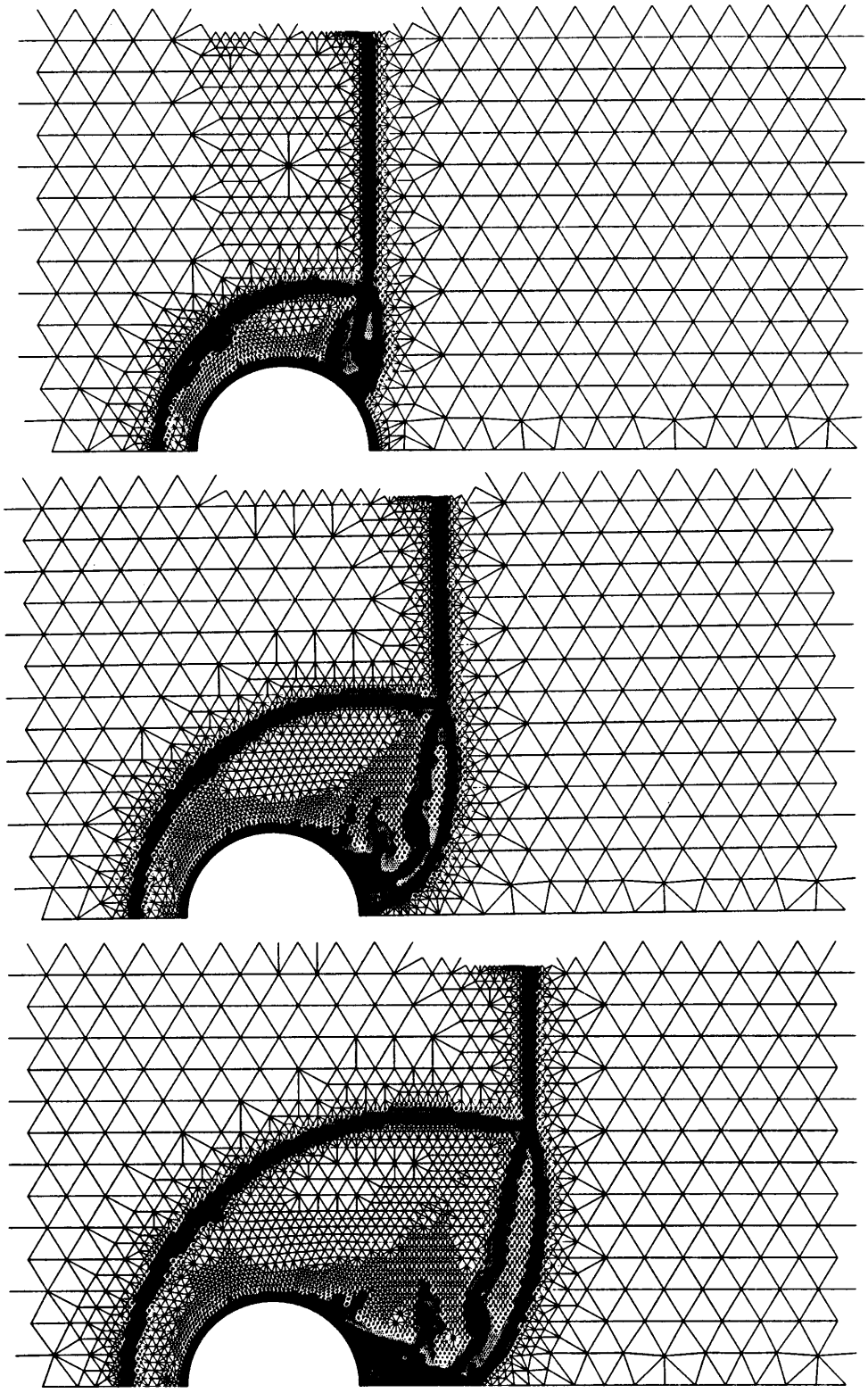

Figure 19. Sequence of adaptive grids at $M_{in} = 5$.

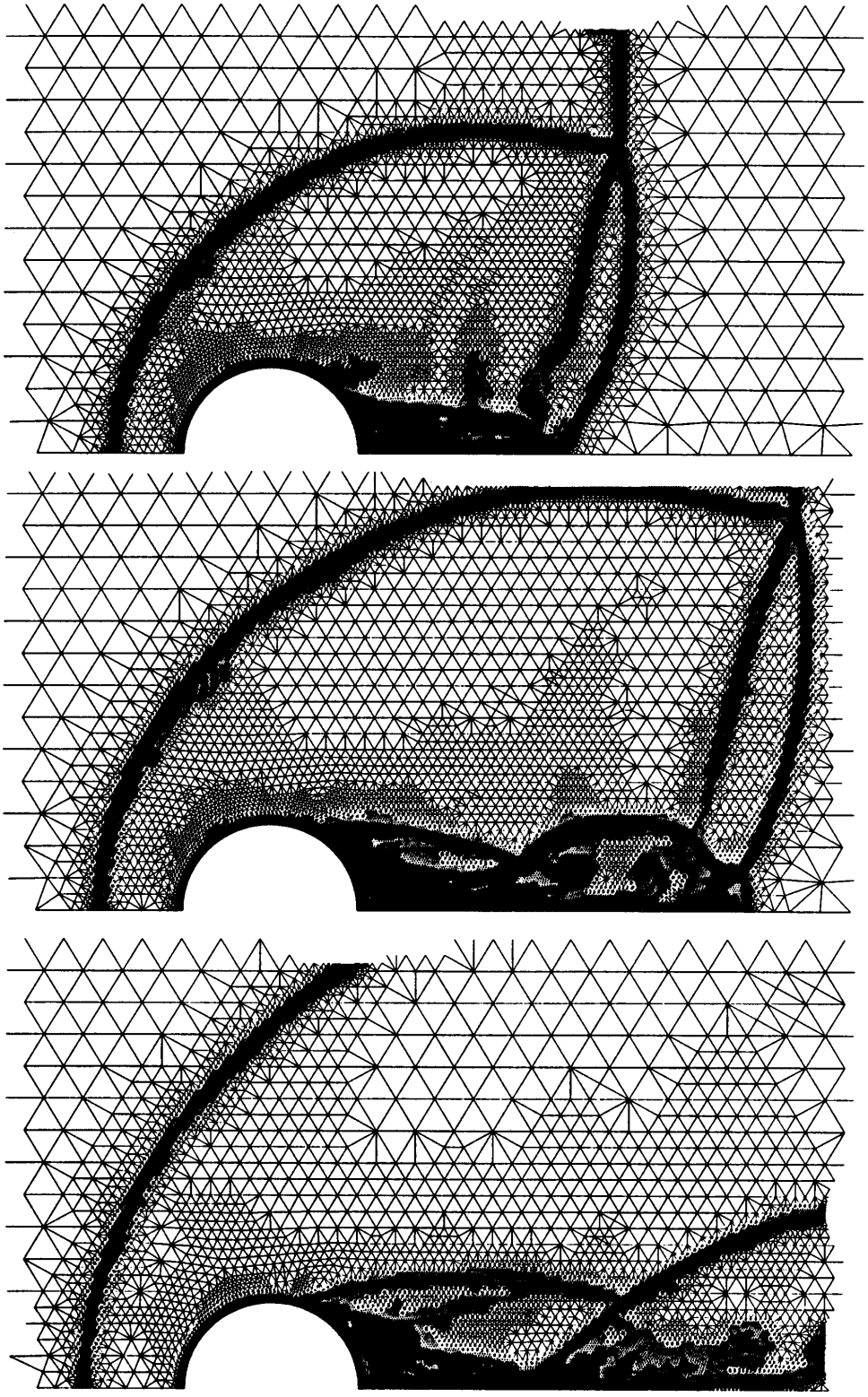

Figure 19. (*Continued*).

at $t_r = 8$ and $t_r = 10$). On the other hand, at $M_{in} = 1{\cdot}7$, large variations of the skin friction occur. These variations are due to the interaction of vortices with the cylinder surface. Finally, the drag history over the cylinder at different Mach numbers is shown in Figure 18. The maximum drag appears at the earlier time instants and is higher at $M_{in} = 1{\cdot}7$. In order to demonstrate the efficiency of the adaptive-grid algorithm in the solution of unsteady gas-dynamic problems, the sequence of the unstructured adaptive-grids at $M_{in} = 5$ is shown in Figure 19. The grid adaptation provides good resolution for both shock waves and slip surfaces. All the calculations have been performed on a HP 9000/650 workstation requiring about 20 h of CPU time.

4. CONCLUSIONS

A numerical study of the propagation of shock waves over a cylinder based on an adaptive Euler/Navier-Stokes method was presented. The method was initially validated against experimental results. Computations were carried out at different Mach numbers and revealed various shock-shock and viscous-inviscid interactions. The conclusions are summarized as follows.

(a) The upper shock system over the cylinder is very similar for all Mach numbers considered in this study. However, the onset of the Mach stem reflection behind the cylinder depends on the incident Mach number.

(b) The viscous-inviscid interactions, as well as the shock structure behind the cylinder, depend on the incident Mach number. The differences are larger when the calculations are carried out for longer time intervals.

(c) Inviscid and viscous calculations provide very similar flow field patterns in the first half of the cylinder. Large differences exist in the second half of the cylinder and the wake of the flow field. These are due to viscous-inviscid interactions.

(d) Large differences between the inviscid and viscous calculations appear in the pressure distribution in the second half of the cylinder.

(e) The present adaptive-grid method provides good resolution in both shock waves and viscous-inviscid interaction phenomena.

Future investigations of the non-stationary, shock–obstacle interaction should include deformation of the obstacle surface as well as turbulent flow effects. In both cases experimental studies do not exist, especially results for validation of CFD methods, and therefore research in this direction should be performed.

ACKNOWLEDGMENTS

The research at UMIST was partially supported by the CEC project COP 94-1239. The authors would like to thank A. O. Galyukov for providing the unstructured grid operator. D. Ofengeim also thanks Dr M. P. Syshchikova and Dr M. K. Beryozkina for several discussions on the topic of shock wave propagation.

REFERENCES

BAUM, J. D. & LÖHNER, R. 1994 Numerical simulation of shock-box interaction using an adaptive finite element scheme. *AIAA Journal* **32,** 682–692.

BERGER, M. J. & OLIGER, J. 1984 Adaptive mesh refinement for hyperbolic differential equations. *Journal of Computational Physics* **53,** 484–512.

BERYOZKINA, M. K., OFENGEIM, D. KH., SYSHCHIKOVA, M. P., TIMOFEEV, E. V., FURSENKO,

A. A. & Voinovich, P. A. 1996 A combined adaptive structured/unstructured technique for essentially unsteady shock–obstacle interactions at high Reynolds numbers. In *Proceedings of the 5th International Conference on "Hyperbolic Problems: Theory, Numerics, Applications"* (eds J. Glimm, J. W. Grove, M. J. Graham & B. Plohr), pp. 464–470, University at Stony Brook, NY, U.S.A., World Scientific Publishers.

Bryson, A. E. & Gross, R. W. F. 1961 Diffraction of strong shocks by cones, cylinders and spheres. *Journal of Fluid Mechanics* **10,** 1–16.

Colella, P. & Glaz, H. M. 1985 Efficient solution algorithms for the Riemann problem for real gases. *Journal of Computational Physics* **59,** 264–289.

Drikakis, D. & Tsangaris, S. 1993 On the accuracy and efficiency of CFD methods in real gas hypersonics. *International Journal Methods in Fluids* **16,** 759–775.

Fursenko, A. A., Sharov, D. M., Timofeev, E. V. & Voinovich, P. A. 1995 An efficient unstructured Euler solver for transient shocked flows. In *Proceedings of the 19th International Symposium on Shock Waves,* Vol. 1, pp. 371–376, Marseille, France.

Glass, I. I. & Sislian, J. P. 1994 *Nonstationary Flows and Shock Waves.* Oxford, U.K.: Clarendon Press.

Glass, I. I., Kaca, J., Zhang, D. L., Glaz, H. M., Bell, J. B., Trangenstein, J. A. & Collins, J. P. 1989 Diffraction of planar shock waves over half-diamond and semicircular cylinders: an experimental and numerical comparison. In *Proceedings of the 17th International Symposium on Shock Waves and Shock Tubes,* pp. 246–25.

Glaz, H. M., Colella, P., Glas, I. I. & Deschambault, R. L. 1985 A numerical study of oblique shock-wave reflections with experimental comparisons. *Proceedings of the Royal Society* A **398,** 117–140.

Harten, A. 1983 High resolution schemes for hyperbolic conservation laws. *Journal of Computational Physics* **43,** 357–393.

Heilig, W. H. 1960 Diffraction of a shock wave behind a cylinder. *Physics of Fluids* supp. I, I–154–157.

Kaca, J. 1988 An interferometric investigation of the diffraction of a planar shock wave over a semicircular cylinder. UTIAS Technical Note 269, University of Toronto, Canada.

Löhner, R. 1987 The efficient simulation of strongly unsteady flows by the finite element method. AIAA Paper 87-0555.

Löhner, R., Morgan, K., Vahdaty, M., Boris, J. P. & Book, D. L. 1988 FEM-FCT: combining unstructured grids with high resolution. *Communications on Applied Numerical Methods* **4,** 717–730.

Ofengeim, D. Kh., Syshchikova, M. P., Beryozkina, M. K., Sharov, D. M. & Voinovich, P. A. 1993 Some features of the transient relaxation to steady-state pressure on the surface of a cylinder acted on by a shock wave. Technical Physics Letters **19**(7).

Roe. 1981 Approximate Riemann solvers, parameters, vectors and difference schemes. *Journal of Computational Physics* **43,** 357–372.

Syshchikova, M. P., Beryozkina, M. K. & Semenov, A. N. 1967 The flow formation around a body in a shock tube. In *Collection of papers: The Aerophysical Investigation of Supersonic Flows,* pp. 7–13. Moscow: Science Publisher (in Russian).

Takayama, K. & Kawauchi, T. 1979 The transition from regular to Mach reflection in truly non-stationary flows. *Journal of Fluid Mechanics* **100,** 147–160.

Takayama, K. & Itoh, K. 1985 Unsteady drag over cylinders and aerofoils in transonic shock tube flows. In *Proceedings of the 15th International Symposium on Shock Waves and Shock Tubes,* pp. 439–485, Stanford, California, U.S.A.

Whitham, G. B. 1957 A new approach to problems of shock dynamics. Part I: Two-dimensional problems. *Journal of Fluid Mechanics* **2,** 145–171.

Woodward, P. R. & Colella, P. 1984 The numerical simulation of two-dimensional fluid flow with strong shocks. *Journal of Computational Physics* **51,** 115–173.

Yang, J. Y., Liu, Y. & Lomax, H. 1987 Computation of shock wave reflection by circular cylinders. *AIAA Journal* **25,** 683–689.

Yang, X., Eidelmann, S. & Lottati, I. 1993 Shock-wave reflection over a semicircular cylinder in a dusty gas. *AIAA Journal* **31,** 1737–1743.